3-D TCAD Methodology for Simulating Double-Hysteresis Filamentary *I–V* Behavior and Holding Current in ESD Protection SCRs

Hasan Karaca, Steffen Holland, Hans-Martin Ritter, Vasantha Kumar, Guido Notermans, *Senior Member, IEEE*, and Dionyz Pogany, *Member, IEEE*

***Abstract*— Current filament (CF)-related double-hysteresis *I–V* behavior and holding current, I_{HOLD}, are analyzed using experiments and 3-D technology computer-aided design (TCAD) simulation in silicon-controlled rectifiers (SCR) for system-level electrostatic discharge (ESD) protection. Our 3-D TCAD methodology uses up and down quasi-dc current sweeps to reveal a memory effect in the current density distribution along the device width. I_{HOLD} is related to the smallest possible CF where the self-sustaining SCR action takes place during down current sweep. I_{HOLD} exhibits a nontrivial dependence on device width, depending on whether a CF is created or not. Analyzing devices of different layouts shows that I_{HOLD} values determined from experiments and 3-D TCAD are almost layout-independent and substantially lower than those evaluated from 2-D TCAD. I_{HOLD} calculated by 3-D TCAD in edge-terminated devices is higher than that in 3-D structures obtained from simple width-extended 2-D doping profiles. The use of latter devices, thus, simplifies the 3-D TCAD *I–V* analysis and provides a safe margin for I_{HOLD} prediction. The work is relevant for designing the latch-up immunity of ESD protection devices, and it also shows that conventional 2-D TCAD can provide unwanted overestimation of I_{HOLD}.**

***Index Terms*— 3-D technology computer-aided design (TCAD) simulation, current filamentation, double-hysteresis *I–V*, electrostatic discharge (ESD) protection, emission microscopy (EMMI), holding current, latch-up immunity, silicon controlled rectifier (SCR), SCR triggering.**

Manuscript received April 26, 2021; revised June 14, 2021; accepted July 13, 2021. Date of publication August 5, 2021; date of current version August 23, 2021. The review of this article was arranged by Editor C. Duvvury. *(Corresponding authors: Hasan Karaca; Dionyz Pogany.)*

Hasan Karaca and Dionyz Pogany are with the Institute of Solid State Electronics (FKE), Vienna University of Technology (TU Wien), 1040 Vienna, Austria (e-mail: hasan.karaca@tuwien.ac.at; dionyz.pogany@tuwien.ac.at).

Steffen Holland, Hans-Martin Ritter, and Vasantha Kumar are with Nexperia Germany GmbH, 22529 Hamburg, Germany (e-mail: steffen.holland@nexperia.com; hans-martin.ritter@nexperia.com; vasantha.kumar@nexperia.com).

Guido Notermans, retired, was with Nexperia Germany GmbH, 22529 Hamburg, Germany. He resides in Berlin, Germany (e-mail: guido.notermans@ieee.org).

Color versions of one or more figures in this article are available at https://doi.org/10.1109/TED.2021.3100301.

Digital Object Identifier 10.1109/TED.2021.3100301

I. Introduction

DUE to their high electrostatic discharge (ESD) robustness, silicon-controlled rectifiers (SCRs) are suitable devices for ESD protection [1], [2]. For system-level ESD protection, discrete devices on low-doped or silicon-on-insulator (SOI) substrate are often used due to their low capacitance, which makes them suitable for high-frequency or large bitrate applications [3], [4]. For latch-up safe operation, high holding voltage, V_{HOLD}, and high holding current, I_{HOLD}, are often requested [5], [6]. While V_{HOLD} has been studied extensively [6], [7], there is less literature related to I_{HOLD} optimization [8]–[10]. Design measures to increase I_{HOLD} have been studied by 2-D technology computer-aided design (TCAD) simulation [8], [9].

It is known that, in sufficiently wide structures, inhomogeneous current density distribution (here called current filaments (CFs) [11]) over the device width can emerge due to negative differential resistance (NDR)–induced instability [12]. This phenomenon cannot be treated by 2-D simulation [13], [14]. The filamentary *I–V* curve has typically a *double-hysteresis* behavior, which has been observed experimentally in power thyristors [15], [16] and ESD protection devices [11], [17]. The origin of the double-hysteresis *I–V* behavior is comprehensively explained in the introductory part of [11] and references therein. The theoretical approaches [12], [18] can qualitatively model the filamentary *I–V* curve and the hysteresis behavior for simple structures with 1-D doping profile extended in the width direction [15], [16]. These works also analyze the current filamentation in power thyristors in relation to device parameters [15], [16]. However, ESD protection devices typically have a complex 2-D cross section, and the analytical analysis would be difficult or even impossible to perform. A 3-D TCAD analysis of grounded-gate MOSFETs has demonstrated differences between the *I–V* curves calculated by 3-D and 2-D TCAD simulations [13], [19]. The values of V_{HOLD} and I_{HOLD} are, thus, expected to be different, depending on whether they were calculated by 2-D and 3-D TCAD. To the best of our knowledge, neither double-hysteresis behavior has been simulated previously in ESD protection devices nor has 3-D TCAD been applied to the I_{HOLD} analysis.

What complicates matters even more is the fact that ESD protections are usually laid out as multifinger devices [20], [21]. I–V curves with multiple branches have been observed in multifinger ESD protection and power devices [17], [22], [23]. However, while the trigger current scales with the number of fingers, the holding current is determined from the activity of the last triggered finger when sweeping the current down [17], [22]. Therefore, it is the behavior of a single finger, which determines I_{HOLD}.

In this article, we present a 3-D TCAD methodology to investigate the *double-hysteresis* filamentary I–V behavior in single-finger ESD protection SCRs and apply it to the determination of I_{HOLD}. The essence is to calculate the I–V characteristics from quasi-dc up and down current sweeps and to determine I_{HOLD} as the smallest current where the SCR is still in the ON-state during the down sweep. I_{HOLD} is analyzed as a function of layout parameters. Simulations are compared to experimental results. We will show that I_{HOLD} determined from 3-D TCAD is substantially lower than that determined from the 2-D TCAD. This has practical relevance for protection design and excludes 2-D TCAD as a tool for reliable I_{HOLD} estimation.

The article is organized as follows. Section II presents devices as well as experiments. Section III introduces the simulation approach. Relation of filamentary I–V curves to current density distribution over the width and the dependence of I_{HOLD} on layout parameters are presented and discussed in Section IV, followed by conclusions in Section V.

II. Devices Studied and Experimental Details

Fig. 1(a) represents a simplified cross section of the studied SCRs. The structures are fabricated on low p-doped silicon on an insulated substrate. The shallow p^+, n-well, and deep p-well under the Signal terminal serve as emitter (E), base (B), and collector (C) of the p-n-p transistor, respectively. The n-well serves also as a substrate resistance of the p-n-p. The n^+-contact to the n-well is short-circuited with the p^+-emitter by metallization. The highly doped n^+-regions of the Ground terminal, p^--substrate/deep p-well, and n-well form the E, B, and C regions of the n-p-n, respectively. Since the p^--substrate and the deep p-well are left floating, we call this device a floating-base SCR. The device is isolated at sides by a shallow trench insulation (STI). Thus, the left and right boundaries in Fig. 1(a) represent the position where STI starts. Although the devices studied here are not exactly identical to those in [24], their basic structure and operation are similar. Devices of different widths W and layout parameters L and L_{pn}, were investigated [see Fig. 1(a)]. The default device parameters are denoted by L_0 and $L_{\mathrm{pn},0}$.

DC I–V curves were recorded in current controlled-mode using a Keithley 2410 source measurement unit or HP 4155A semiconductor parameter analyzer. Up and down sweeps are used to record the double-hysteresis I–V curve. To monitor the current distribution over the device width as a function of total current, emission microscopy (EMMI) [21], [25], [26] has been applied simultaneously to I–V recording. The EMMI pattern is recorded from the polished backside of the chip by an infrared camera [17].

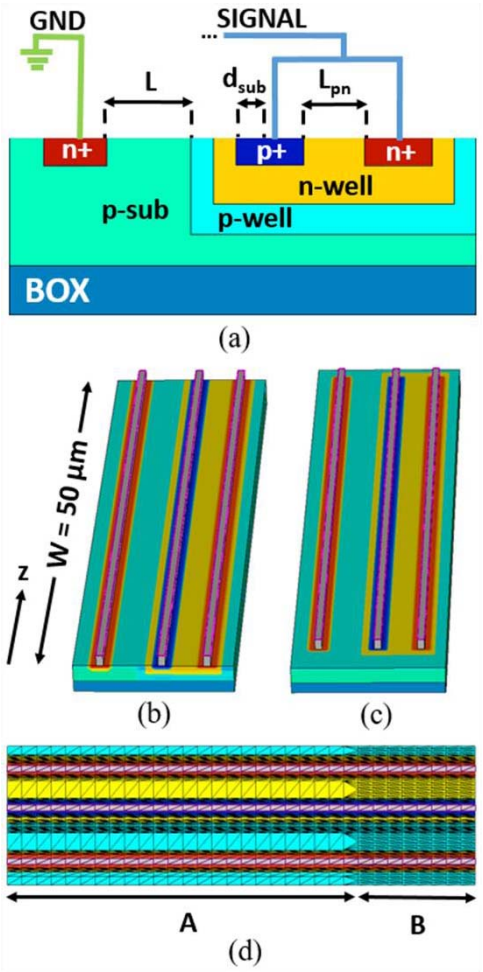

Fig. 1. (a) Simplified cross section of the studied device with indicated layout parameters. Devices used in 3-D TCAD analysis with (b) width-extended 2-D profile and (c) edge termination. (d) Example of standard mesh region (A) and region with finer mesh (B).

III. TCAD Simulation Approach

Current density distribution and I–V curves of SCRs are simulated by TCAD using Synopsys Sentaurus [27]. Isothermal drift-diffusion simulation is employed since the self-heating effect at the applied low currents is negligible (see Appendix). *Up* and *down* current sweeps in 3-D TCAD with a rate of ± 50 mA/s are used to produce the quasi-dc I–V curve and reveal the possible hysteresis behavior. Since the solution at the next iteration step depends on the previous distribution of internal state parameters, such as current densities, carrier concentrations, and electrical potential, the device prehistory is well taken into account. In particular, we have monitored the current density distribution along the device width at particular points in the up and down I–V curves in order to check whether CF was created when entering the NDR region or not. The NDR is necessary but not sufficient condition to create CF [15], [16] (see more details related to meshing in the following and Section IV). The above is the main approach corresponding to our TCAD methodology.

The layouts of the 3-D simulation structures are presented in Fig. 1(b) and (c).

1) A structure where the 2-D profile is extended in the width (i.e., z-axis) direction, called here as

"width-extended" structure [see Fig. 1(b)], to study variations in different W's, L's, and L_{pn}'s. An example of a top view of the mesh is given in Fig. 1(d).

2) A structure with edge terminations [see Fig. 1(c)], which resembles the real structure and is called "terminated" device, to investigate the effects of edges on the I–V curves.

The lateral boundaries of this structure represent positions where STI surrounds the device.

The Neumann boundary conditions are applied at all six sides of the simulation region. Thus, the effect of STI surrounding is covered.

To create CF when entering the NDR region in a wide enough device, two conditions have to be fulfilled: The device width has to be larger than about 5× the CF wall thickness L_{CF} [18], and there should be an inhomogeneity along the width, which is larger than L_{CF} [15], [16]. In our case, L_{CF} was about 9 μm (see the exact definition of L_{CF} in Section IV). In most of the simulations, the natural mesh asymmetry created by the mesh generator [such as in region A in Fig. 1(d)] was sufficient to induce a large enough inhomogeneity to create a filamentary state in a wide device. In some cases, in order to induce the filamentary instability in devices with $W > 50$ μm, it was necessary to introduce an "inhomogeneity" into the mesh, which is, in our case, a region of about 12-μm width with a finer mesh [see region B in Fig. 1(d)]. Thus, the widths of both regions A and B are larger than L_{CF} fulfilling the second condition for CF creation. The width of region B is the same for all W values and both the width-extended and terminated devices. From our experience, the incommensurate ratio of mesh steps in z-direction in regions A and B helps the convergence to stable filamentary solution. Thus, our approach in mesh selection with respect to CF creation when entering the NDR region can be summarized as follows: if CF is not created for the wide enough devices ($W \gg 45$ μm) with mesh of type A, we introduced the region B. The finer the mesh in the A and B regions, the longer is the computational time. The mesh presented in Fig. 1(d) provided sufficiently accurate and stable results. We emphasize that the basic property of CF, such as L_{CF} and general shape of filamentary I–V curve, does not depend much on meshing details. The mesh size determines just their accuracy. In particular, the SCR properties in the ON-state (such as I_{HOLD} value) are quite insensitive on meshing. The more detailed analysis of the meshing problem is out of the scope of this article and will be addressed in future work.

The simulation model is not calibrated in detail, so there is a small deviation between the experimental and simulated I–Vs. Our purpose is to concentrate on qualitative tendencies. For the reason of comparison, we have also performed the I–V simulation using a 2-D TCAD with a current ramp of 50 mA/s (rising slope). There, the simulation structure was based on the 2-D cross section profile given in Fig. 1(a).

IV. Results and Discussion

A. Double-Hysteresis I–V Behavior and I_{HOLD}

Fig. 2(a) and (b) shows the measured full-scale and zoomed dc I–V curves, respectively, recorded during the up and down sweeping in a device with $W = 124$ μm. Curve "3-D" in Fig. 3(a) and (b) shows the up and down sweeps of the 3-D TCAD simulated I–V curve in full and zoomed voltage scales, respectively. The I–V curve "2-D" in Fig. 3 represents a 2-D I–V behavior with homogeneous current flow over the width in the NDR region. Remarkably, the I–V curves in Figs. 2 and 3 (curve "3-D") both exhibit a *double-hysteresis* I–V behavior. While the lower hysteresis is well pronounced [see Figs. 2(a) and 3(a)], the upper one [see encircled regions in Figs. 2(a) and 3(a) zoomed in respective Figs. 2(b) and 3(b)] might be overlooked in the scale of Figs. 2(a) and 3(a).

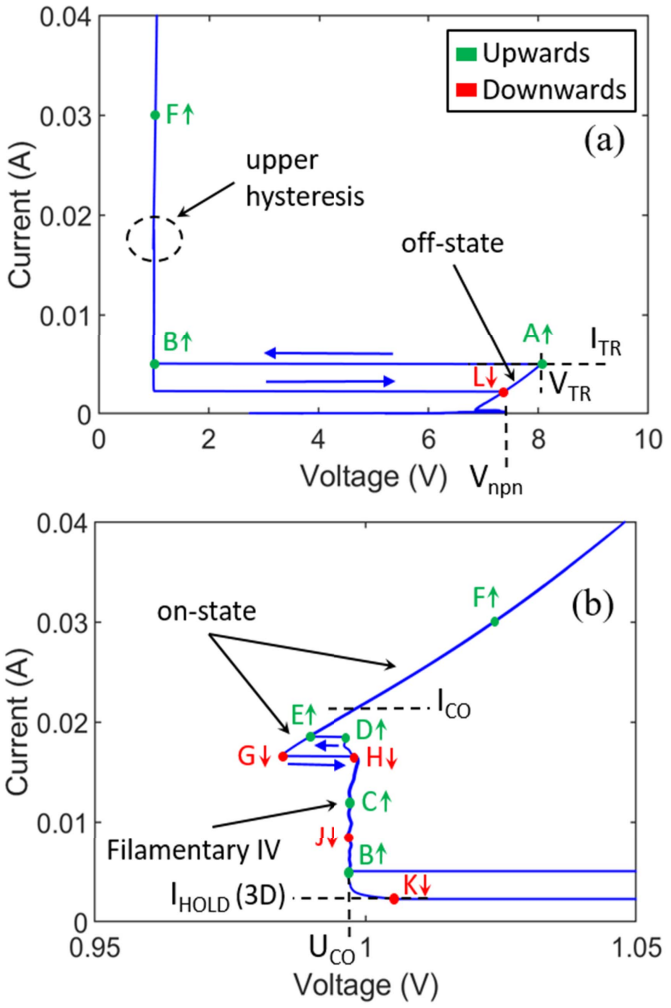

Fig. 2. Experimental I–V curves for a device with standard layout parameters and $W = 124$ μm. (a) overall and (b) zoomed-in views. The points A–K indicate the device state at which EMMI images in Fig. 4 were recorded. The current sweeping direction is indicated by arrows and color.

Fig. 4 shows the EMMI pattern for selected points on the I–V curve from Fig. 2. Fig. 5 shows the 3-D plots of current density distributions for the selected points on the simulated I–V curve in Fig. 3. The points are labeled identically in Figs. 2 and 3 according to the same qualitative behavior. However, the exact values of current and voltage can slightly differ. To clearly see the current distribution in the z-direction, current density values across the line Ω–Ω' [depicted in Fig. 5(a)] were extracted and plotted in Fig. 6.

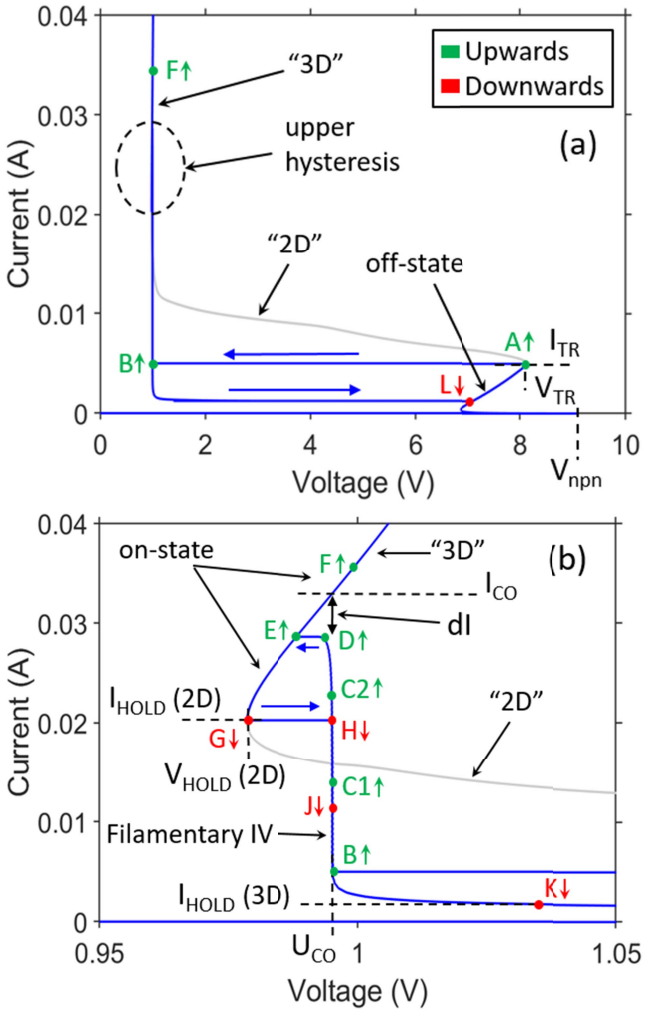

Fig. 3. Simulated 3-D *I–V* characteristics (curve "3-D") in (a) full and (b) zoomed scales for a device with standard layout parameters and $W = 124\ \mu$m. The labels A–K indicate the working points at which $J(z)$ distribution was extracted in Fig. 6. The ON-state, OFF-state and filamentary parts of the *I–V* curve are indicated. The arrows indicate the sweeping direction of the current. Curve "2-D" represents the 2-D *I–V* behavior with the homogeneous current flow.

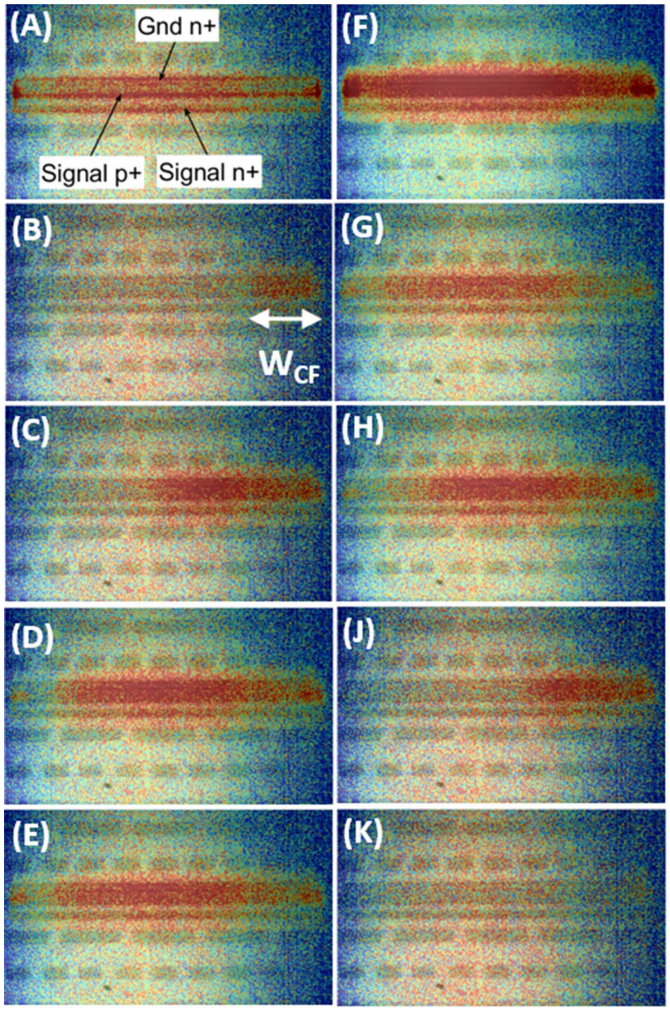

Fig. 4. EMMI images at working points A–K from Fig. 2, aligned with backside reflectivity image of the device. In B, the CF width W_{CF} is indicated.

At low currents of below 100 μA, a small voltage peak at about $V = 7.5$ V (labeled V_{npn}) is observed in the measured $I–V$ curve in Fig. 2(a). It is due to avalanching and snapping-back of the open base n-p-n, which is qualitatively well reproduced by simulations [see Fig. 3(a)]. The n-p-n snap-back is related to the current-dependent transistor gain [28]. A small discrepancy in the V_{npn} voltage in Figs. 2(a) and 3(b) is due to the noncalibrated model. The n-p-n at these small currents is turned on homogeneously over the width. We suppose that the filamentary instability due to NDR in the n-p-n is not developed due to very low current density under these conditions.

While the total current increases from zero up to the trigger current I_{TR}, current flows mostly via n-well substrate resistance of the p-n-p [cf. Fig. 1(a)] and the SCR remains in the OFF-state. The OFF-state current flows homogeneously over the entire width [see EMMI in Fig. 4A and $J(z)$ in Fig. 6 (curve A)]. In Fig. 3, we observe the same 3-D and 2-D $I–V$ behavior below I_{TR} due to homogeneous current flow in this regime.

When the lateral potential drop across the p^+/n-well junction at Signal is sufficiently high, the p-emitter starts to inject, which drives the device into the NDR region and causes the voltage snapback at $I = I_{TR} \approx 5$ mA [point B in Figs. 2(a) and 3(a)]. Since the simulated device is large enough ($W \gg L_{CF}$), a CF can develop, resulting in the vertical or filamentary $I–V$ curve at the so-called coexistence voltage U_{CO}, Figs. 2(b) and 3(b) [11], [15]. The experimental U_{CO} is accurately reproduced by 3-D TCAD. Note that U_{CO} is higher than the holding voltage in the device with homogeneous current flow, V_{HOLD} (2-D) (see Fig. 3(b) and [11]). The emission pattern and $J(z)$ at point B are shown in Fig. 4B and Fig. 6 (curve B), respectively. The width of this initial CF W_{CF} of 29 μm from experiments and 20 μm from the simulation is consistent with its estimation from I_{TR}/J_{CO}, where $J_{CO} = I_{CO}/W$ is about 0.17 and 0.25 mA/μm, respectively. J_{CO} is the 1-D current density, which is current independent along the filamentary $I–V$ branch [11]. The CF in simulations of Fig. 6 (curve B) is created and pinned at the right boundary,

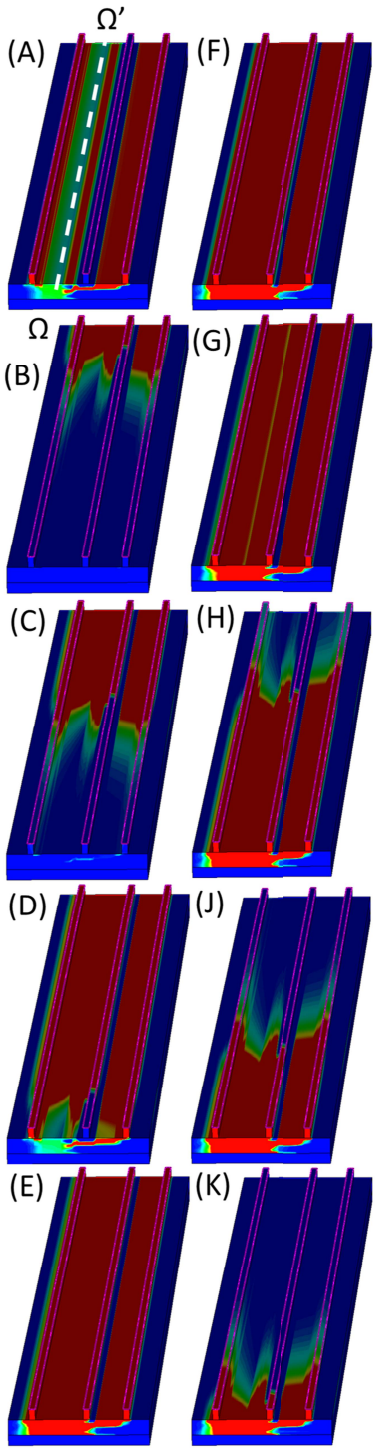

Fig. 5. 3-D TCAD simulated total current density distribution in width-extended device at working points A–K, from Fig. 3. In (C), the working point corresponds to C1 in Figs. 3 and 6. The $J(z)$ distribution is extracted along lines as Ω–Ω′ indicated in (A).

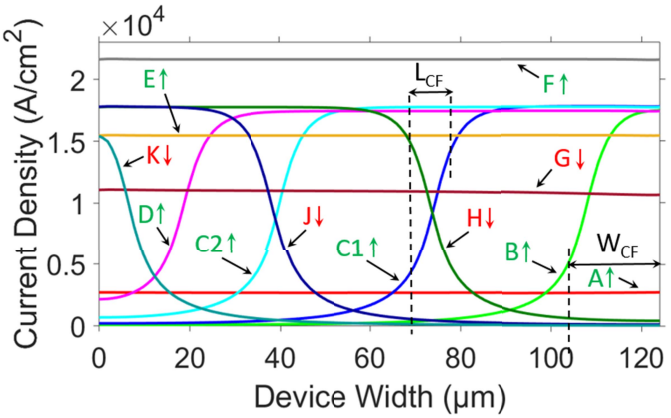

Fig. 6. Extracted distribution of simulated total current density along the device width at different working points (A–K) from Fig. 3. The $J(z)$ distributions are extracted from data of Fig. 5, along lines such as Ω–Ω′ in Fig. 5A. The filament width W_{CF} is indicated in curve B. The filamentary wall thickness L_{CF} is indicated in curve C1.

but a CF creation at the left one is also possible if mesh of type A is used over the whole device width. If a mesh of type B is used, then the filament originates at the side of mesh type A since this region is wider than region B and the CF can develop there more easily [15], [16].

At U_{CO}, the ON-state region with the high current density $J_{CO} = I_{CO}/W$ (i.e., inside the CF) coexists with a low current density OFF-state elsewhere. The $J(z)$ distribution can be directly related to the distribution of the B–E voltage of the p-n-p transistor, which controls the SCR action. The ON- and OFF-state regions in the CF are separated by a transition region called the filamentary wall having the thickness of L_{CF} (see Fig. 6 and [11], [15], and [18]). According to the model in [15] and [16], L_{CF} is an increasing function of the conductivity of SCR base (in our case the n-well) and a complex function of transistor gains. The value of U_{CO} is determined by the balance between the ON- and OFF-state regions at the filamentary wall [15], [16], [18].

Figs. 4C and 6 (curves C1 and C2) show the increase in W_{CF} with increasing current I according to

$$W_{CF} \approx \frac{I}{J_{CO}} \tag{1}$$

where J_{CO} remains constant.

At still higher current (point D), the CF wall reaches the device end, and the inhomogeneous filamentary state becomes unstable. The current conduction reverts to a homogeneous state and the voltage jumps to point E. The voltage jump D → E represents an "energy gain" related to the disappearance of CF wall [11], [15]. The current difference dI between point D and the point at the ON-state I–V curve at U_{CO} [see Fig. 3(b)] is related to a missing current flow over the region with a thickness of L_{CF} nearly.

Above point E, the current flows homogeneously [see Figs. 4F and 6 (curve F)]. When the current decreases, the homogeneous current distribution stays stable until the point G [see Figs. 4G and 6 (curve G)]. Notice that the 3-D I–V (curve "3-D") and 2-D I–V (curve "2-D") characteristics in Fig. 3(b) are identical in the homogeneous ON-state. The upper hysteresis HDEG [see Fig. 3(b)] originates because, at point D, the parameter dI is related to L_{CF}, while, at point G, the device enters the NDR region, which depends on the shape of the 2-D I–V curve. These two SCR characteristics are not directly related to each other [15], [16]. At the current region of the upper hysteresis, there may exist two different voltages for the same applied current depending

on whether the device conducts homogeneously over the width (region G–E), or CF is created (H–D). These two states depend on sweeping prehistory.

Below point G, the device enters the NDR region, and a CF is created. The voltage jumps to point H on the filamentary I–V curve. The EMMI and $J(z)$ patterns at point H show the pronounced filamentary state [see Figs. 4H and 6 (curve H)]. Interestingly, in this simulation, the CF at point H is pinned at the left boundary, which is the opposite side of the device compared to the side that the current rose initially (compare curves H and B–D in Fig. 6). In this particular case, the position of mesh type B coincides with the CF position. However, the CF can be pinned also at the right boundary, depending on mesh details, current step, and so on, indicating that numerical nuances matter. However, what is important is that the CF is always created for devices larger than 50 μm (so for $W > 5 \times L_{CF}$) at either the left or right positions, and so a stable filamentary solution is obtained.

When the current decreases further, W_{CF} decreases (see data in Figs. 4 and 6 for point J) until point K, the current called 3-D I_{HOLD}, or I_{HOLD} (3-D). Notice that the voltage at point K is only slightly higher than U_{CO}; consider the apparent amplifying effect of the zoomed scale in Figs. 2(b) and 3(b). At this point, the filamentary I–V curve enters its unstable branch (see line "F" in Fig. 1 in [11] for details). I_{HOLD} (3-D) is the lowest current where the SCR still operates in the ON-state. We emphasize that this is the I_{HOLD} value that has to be considered in latch-up considerations. The EMMI and $J(z)$ in Figs. 4 and 6, respectively, show a small CF at the structure edge at working point K. Its width W_{CF} is determined by L_{CF}. L_{CF} estimation from I_{HOLD} (3-D)/$J_{CO} \approx$ 9 μm is consistent with the 20%–80% variation in $J(z)$ (see Fig. 6). Due to the filamentary nature of conduction, I_{HOLD} (3-D) of about 2 mA is much lower than I_{HOLD} (2-D) $\approx$ 20 mA. However, the current density inside the CF of nearly $J_{CO} = 0.25$ mA/μm is higher compared to that at I_{HOLD} (2-D) of I_{HOLD} (2-D)/$W \approx 0.16$ mA/μm. This shows that the SCR action in CF at I_{HOLD} (3-D) is supported by a sufficiently high current density.

Below point K, the self-sustaining operation of SCR in the CF is not possible anymore, and the device returns to a mode where the current only flows through the open base n-p-n [see point L in Figs. 2(a) and 3(a)], where the current flows again homogeneously (not shown).

We remark that the lower hysteresis LABK (see Fig. 3) is due to the fact that, while I_{TR} at point A is related to homogeneous current flow in the OFF-state, the property of the SCR at point K is related to the filamentary state.

B. Geometry Dependence of I_{HOLD}

The theory predicts that the filamentary instability occurs in devices wider than about $5 \times L_{CF}$ [18], which is about 45 μm in our case. Therefore, we have carried out I–V measurements of available devices with W in the 31.3–185.8-μm range, and we performed simulations of both types of devices (width-extended and terminated) with W in the 2–185-μm range. Thus, both regimes below and above $5 \times L_{CF}$ are covered.

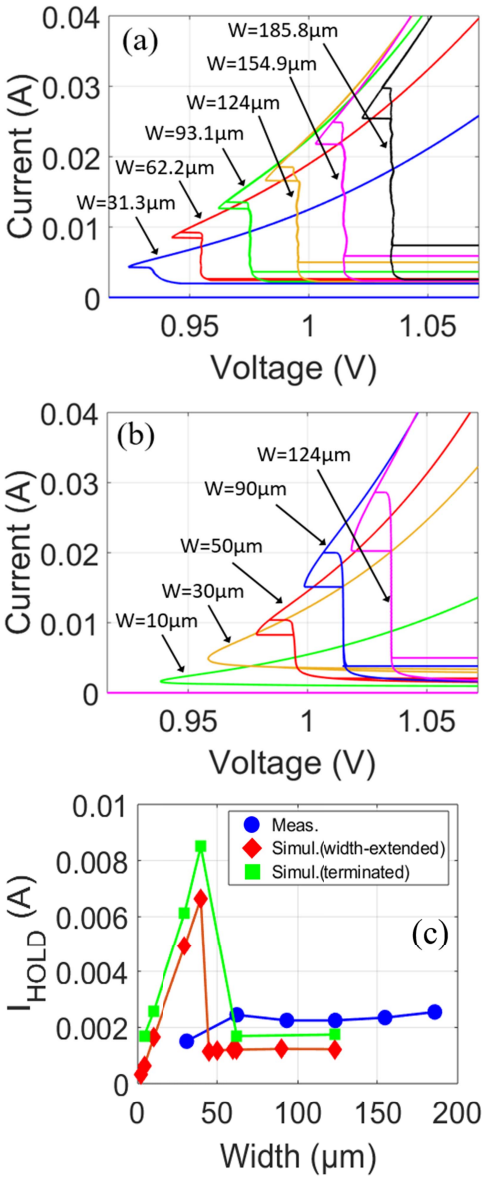

Fig. 7. (a) Experimental and (b) 3-D TCAD simulated I–V curves for the width-extended device with the device width W as a parameter. For better visibility, the curves in (a) and (b) are fanned out with a 20-mV distance between two curves. The V_{CO} value for each curve does not depend on the device width W. (c) Measured and simulated I_{HOLD} values extracted from data of (a) and (b). The data points for the terminated device are also included. In the case of no CF creation for $W < 50$ μm, the value of I_{HOLD} (2-D) is considered for I_{HOLD}.

Examples of experimental and 3-D-simulated I–V curves for width-extended devices are given in Fig. 7(a) and (b), respectively. For better visibility, the curves for increasing width are subsequently horizontally fanned out with a 20-mV distance between two curves. This means that the U_{CO} value does not depend on the device width W. The I_{HOLD} values extracted from the I–V data of Fig. 7(a) and (b) are given in Fig. 7(c). In experiments, I_{HOLD} for $W = 31.3$ μm is slightly smaller than the values for $W > 60$ μm, which are width-independent. The simulated I_{HOLD} (3-D) shows, first, a linear increase with W until $W = 40$ μm, and then, it jumps to a constant value for $W > 45$ μm. For $W < 45$ μm, the device

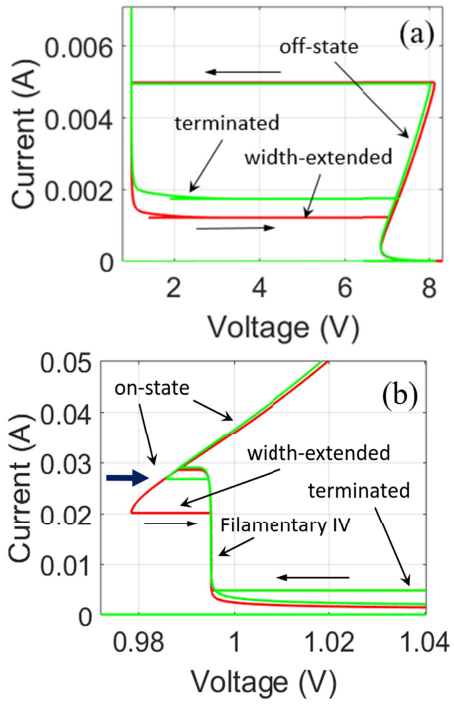

Fig. 8. 3-D TCAD simulated I–V curve in width-extended and terminated device in (a) full and (b) zoomed scales. $W = 124$ μm. The thick arrow in (b) indicates the early transition from ON-state to filamentary state in the terminated device. The small horizontal arrows indicate the current sweeping direction.

is not large enough to induce the NDR instability, which is consistent with the $5 \times L_{CF}$ criterion. For $W < 45$ μm, the values of I_{HOLD} from 2-D and 3-D TCAD are identical, and thus, I_{HOLD} scales linearly with W. This can be directly seen in the I–V curves where the double-hysteresis and ideal filamentary I–V behavior is not formed for the device with $W = 31.3$ μm in experiments [see Fig. 7(a)] and for $W = 10$ μm and $W = 30$ μm in simulations [see Fig. 7(b)]. Thus, the double-hysteresis filamentary I–V in Fig. 7(a) and (b) is observed only for $W > 5 \times L_{CF}$. We notice that the lack of devices with widths in the 30–50-μm range prevents us to see the linearly increasing part in the I_{HOLD}–W dependence in the experimental data.

Fig. 8 compares the 3-D I–V curves of the width-extended and terminated structure for $W = 124$ μm. While the trigger parameters are nearly identical for this width [see Fig. 8(a)], I_{HOLD} increases by 30% for the terminated device [see Fig. 8(b)]. Furthermore, one observes a transition from the ON-state to filamentary I–V curve at higher currents in the down-sweep than in the terminated device, as indicated by the thick arrow in Fig. 8(b). The termination likely induces an inhomogeneity, which facilitates an earlier transition to the filamentary state.

The simulated I_{HOLD} values in the terminated device as a function of W are added in Fig. 7(c) (see green squares). The critical device width for the CF creation of about 45 μm also fulfills the $5 \times L_{CF}$ criterion. One can remark that I_{HOLD} in the terminated device is higher than that in the width-extended device, and this difference is nearly width-independent for

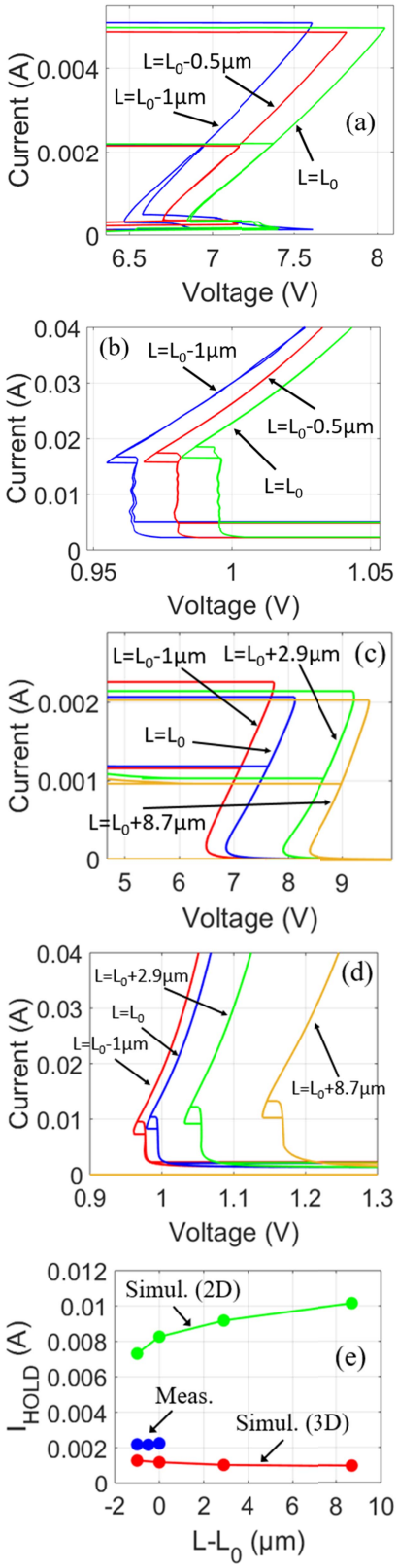

Fig. 9. (a) and (b) Experimental and (c) and (d) 3-D TCAD simulated I–V curves for the width-extended device as a function of (a) L and (c) near V_{TR} and (b) and (d) near U_{CO} voltages. (e) Extracted measured I_{HOLD} and simulated values of I_{HOLD} (3-D) and I_{HOLD} (2-D) as a function of L.

$W > 60$ μm. This is attributed to an additional current flow around the edge. The I_{HOLD} values for terminated devices also match better to experimental values. However, this increased

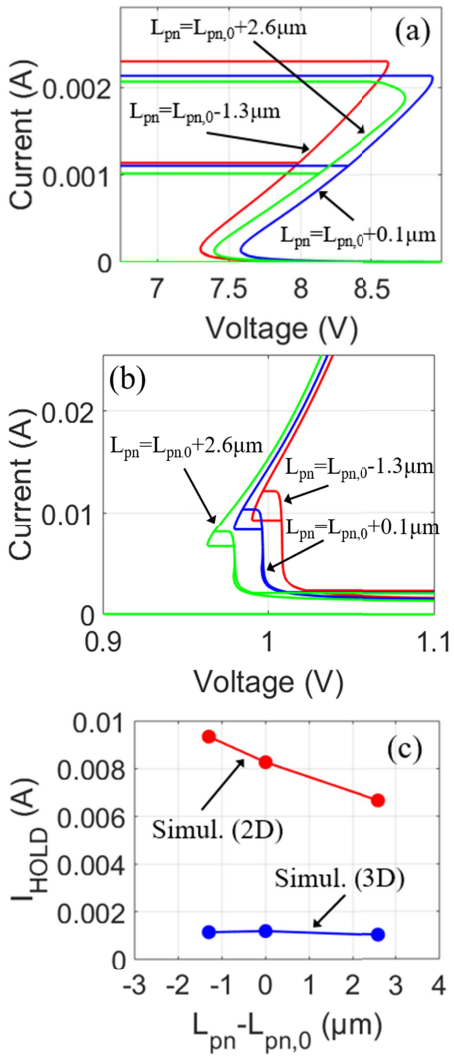

Fig. 10. Simulated 3-D *I–V* curves for the width-extended device in (a) full and (b) zoomed scales with L_{pn} as parameters. (c) Extracted simulated values of I_{HOLD} (3-D) and I_{HOLD} (2-D) as a function of L_{pn}.

accuracy is accompanied by an increased simulation time. Since I_{HOLD} for the width-extended device is lower than for the terminated device, the former represents, thus, the worst case scenario in I_{HOLD} estimation. For the latter and computational time-saving reasons, I_{HOLD} for other layout variations has been evaluated only for the width-extended device with $W = 50\ \mu$m. For this width, a CF is certain to be created.

Fig. 9(a)–(d) shows the experimental and simulated $I–V$ curves with L as a parameter. Fig. 9(a) and (c) shows the $I–V$ curve near the V_{TR} and Fig. 9(b) and (d) near U_{CO}. Since increasing L enhances the base width of the n-p-n, its gain decreases, and the open base breakdown voltage of the n-p-n shifts slightly to higher values. As well, due to the same reason the V_{HOLD} (2-D) shifts to higher voltage with increasing L. U_{CO} follows this trend. This is observed in both experiment and simulation. The extracted values of I_{HOLD} from 2-D and 3-D simulations are given in Fig. 9(e). While I_{HOLD} (2-D) increases with L, I_{HOLD} (3-D) is L-independent and much lower than I_{HOLD} (2-D).

Fig. 10(a) and (b) shows the simulated $I–V$ curves with L_{pn} as a parameter near V_{TR} and near U_{CO}, respectively. For this layout variation, there are no experimental data. The value of I_{TR} for the studied layout range does not depend much on L_{pn} [see Fig. 10(a)]. I_{TR} depends on total n-well resistance below p^+ and in the region of length L_{pn} [see Fig. 1(a)]. However, it is mainly the n-well resistance part of width d_{sub} below the p-well, which controls the forward biasing of the p^+/n-well junction necessary for p-n-p triggering. When a potential drop of about 0.7 V occurs on this resistance part the SCR triggers. Since d_{sub} is L_{pn}-independent and the net n-well doping of this region is lower than that in the region of the length L_{pn}, the value of V_{TR} also does not depend much on L_{pn}. V_{HOLD} (2-D) decreases as L_{pn} increases due to an increased contribution of the vertical p-n-p current path for larger L_{pn}. The vertical current path of the p-n-p is discussed in [24].

The extracted values of I_{HOLD} from 2-D and 3-D simulations are shown in Fig. 10(c). While I_{HOLD} (2-D) decreases with L_{pn}, I_{HOLD} (3-D) is lower and layout-independent.

It is challenging to explain the independence of I_{HOLD} (3-D) on layout parameters in Figs. 9(e) and 10(c) in simple and intuitive terms. In general, we relate it to the high injection condition in the CF (the SCR is in the ON-state there), where the details of geometry do not play a significant role. At high injection, a dense electron-hole plasma floods the entire device active region and controls the transport. In addition, in these floating-base devices, a conductivity modulation takes place in the low-doped p-sub in between the Ground n^+-region and deep p-well [4], [24], which complicates the picture even more. Moreover, although U_{CO}, which is related to I_{HOLD} (3-D), can be modeled analytically only for simple 1-D doping profile structures [15], [16]. There is no theory, and therefore, the intuitive view for how U_{CO} depends on the SCR structure parameters with 2-D doping profiles. The understanding of the complexity of this problem will be treated in future works.

V. Conclusion

Using quasi-dc current *up* and *down sweeps* in 3-D TCAD, we are able to simulate the double-hysteresis $I–V$ curve and holding current I_{HOLD} in ESD protection SCRs. The shape of the $I–V$ curve has been related to spatial distribution of the current density in the width direction. The value of simulated I_{HOLD} in the devices with width-extended 2-D profiles is lower than that in the terminated devices. The simulation of width-extended devices represents, thus, a worst case scenario in the 3-D TCAD estimation of I_{HOLD}. I_{HOLD} increases with the device width for W smaller than five times the filamentary wall thickness since no CFs are formed. For larger W, CFs are formed, and I_{HOLD} becomes W-independent. Importantly, while I_{HOLD} determined from 3-D TCAD is typically independent of the layout parameters, the value of I_{HOLD} determined from 2-D TCAD strongly depends on them and is typically several times higher. Thus, 3-D TCAD has to be used for the latch-up safe ESD protection design of I_{HOLD}.

Appendix

The self-heating effect has been estimated using the 2-D thermodynamic simulation of the structure shown in Fig. 1(a).

STI and the additional silicon on the substrate and the lateral sides have been considered. The substrate thickness was 240 μm, and the lateral chip extension beyond STI was 200 μm on each side. The current density was chosen at $J_{CO} = I_{CO}/W$ [see Fig. 3(b)], which corresponds to that in CF. The simulated maximum temperature rise at steady state was about 15 K, which represents worst case estimate. Since the 2-D simulation considers zero heat flow in the z-direction (i.e., infinite extended heat source in the z-direction), we may expect that the temperature in the 3-D structure with finite width will be even lower.

REFERENCES

[1] J. Di Sarro, K. Chatty, R. Gauthier, and E. Rosenbaum, "Study of design factors affecting turn-on time of silicon controlled rectifiers (SCRS) in 90 and 65 nm bulk CMOS technologies," in *Proc. IEEE Int. Rel. Phys. Symp. Proc.*, San Jose, CA, USA, Mar. 2006, pp. 163–168, doi: 10.1109/RELPHY.2006.251210.

[2] G. Notermans *et al.*, "Design of an on-board ESD protection for USB3 applications," *IEEE Trans. Device Mater. Rel.*, vol. 16, no. 4, pp. 504–512, Dec. 2016, doi: 10.1109/TDMR.2016.2622400.

[3] W. Soldner *et al.*, "RF ESD protection strategies: Codesign vs. low-C protection," *Microelectron. Rel.*, vol. 47, no. 7, pp. 1008–1015, Jul. 2007, doi: 10.1016/j.microrel.2006.11.007.

[4] G. Notermans, H.-M. Ritter, S. Holland, and D. Pogany, "Modeling dynamic overshoot in ESD protections," in *Proc. 40th Electr. Overstress/Electrostatic Discharge Symp. (EOS/ESD)*, Reno, NV, USA, Sep. 2018, pp. 1–9, doi: 10.23919/EOS/ESD.2018.8509781.

[5] S. H. Voldman, *Latchup*. Hoboken, NJ, USA: Wiley, 2008.

[6] M.-D. Ker, S.-F. Hsu, *Transient-Induced Latchup in CMOS Integrated Circuits*. Hoboken, NJ, USA: Wiley, 2009.

[7] Y.-C. Huang and M.-D. Ker, "A latchup-immune and robust SCR device for ESD protection in 0.25-μm 5-V CMOS process," *IEEE Electron Device Lett.*, vol. 34, no. 5, pp. 674–676, May 2013, doi: 10.1109/LED.2013.2252456.

[8] M. P. Mergens, C. C. Russ, K. G. Verhaege, J. Armer, P. C. Jozwiak, and R. Mohn, "High holding current SCRs (HHI-SCR) for ESD protection and latch-up immune IC operation," *Microelectron. Rel.*, vol. 43, no. 7, pp. 993–1000, 2003, doi: 10.1016/S0026-2714(03)00125-2.

[9] H. Liang, X. Bi, X. Gu, H. Cao, and Y. Zhang, "Investigation on LDMOS-SCR with high holding current for high voltage ESD protection," *Microelectron. Rel.*, vol. 61, pp. 120–124, Jun. 2016, doi: 10.1016/j.microrel.2016.01.016.

[10] S. Bart, B. Ilse, M. Olivier, and K. Bart, "On-chip ESD protection with improved high holding current SCR (HHISCR) achieving IEC 8 kV contact system level," in *Proc. IEEE Electr. Overstress/Electrostatic Discharge Symp. (EOS/ESD)*, Reno, NV, USA, Nov. 2010, pp. 1–10.

[11] D. Pogany *et al.*, "Measuring holding voltage related to homogeneous current flow in wide ESD protection structures using multilevel TLP," *IEEE Trans. Electron Devices*, vol. 58, no. 2, pp. 411–418, Feb. 2011, doi: 10.1109/TED.2010.2093143.

[12] H. L. Grubin, V. V. Mitin, E. Schöll, and M. P. Shaw, *The Physics of Instabilities in Solid State Electron Devices*. New York, NY, USA: Springer, 2013.

[13] K. Esmark, "Device simulation of ESD protection elements," Ph.D. dissertation, ETH Zurich, Zurich, Switzerland, 2001, doi: 10.3929/ethz-a-004317494.

[14] M. Denison *et al.*, "Moving current filaments in integrated DMOS transistors under short-duration current stress," *IEEE Trans. Electron Devices*, vol. 51, no. 10, pp. 1695–1703, Oct. 2004, doi: 10.1109/TED.2004.835978.

[15] I. Varlamov, V. Osipov, and E. Poltoratskii, "Current fillamentation in a four-layer structure," *Sov. Phys. Semicond.*, vol. 3 no. 8, pp. 978–982, 1970.

[16] I. V. Varlamov and V. V. Osipov, "Current filamentation in pnpn-structures," *Sov. Phys. Semicond.*, vol. 3, no. 7, pp. 803–911, 1970.

[17] C. Fleury, G. Notermans, H.-M. Ritter, and D. Pogany, "TIM, EMMI and 3D TCAD analysis of discrete-technology SCRs," *Microelectron. Rel.*, vols. 76–77, pp. 698–702, Sep. 2017, doi: 10.1016/j.microrel.2017.06.070.

[18] M. Meixner, P. Rodin, E. Schöll, and A. Wacker, "Lateral current density fronts in globally coupled bistable semiconductors with S- or Z-shaped current voltage characteristics," *Eur. Phys. J. B*, vol. 13, no. 1, pp. 157–168, Jan. 2000, doi: 10.1007/s100510050019.

[19] M. Litzenberger, C. Furbock, D. Pogany, E. Gornik, K. Esmark, and H. Gossner, "Investigation of 3D phenomena in the triggering of gg-nMOS electrostatic discharge protection devices," in *Proc. 30th Eur. Solid-State Device Res. Conf.*, Cork, Ireland, Sep. 2000, pp. 520–523, doi: 10.1109/ESSDERC.2000.194829.

[20] C. Musshoff, H. Wolf, H. Gieser, P. Egger, and X. Guggenmos, "Risetime effects of HBM and square pulses on the failure thresholds of GGNMOS-transistors," *Microelectron. Rel.*, vol. 36, nos. 11–12, pp. 1743–1746, Nov. 1996, doi: 10.1016/0026-2714(96)00188-6.

[21] C. Russ, K. Bock, M. Rasras, I. De Wolf, G. Groeseneken, and H. E. Maes, "Non-uniform triggering of gg-nMOSt investigated by combined emission microscopy and transmission line pulsing," in *Proc. Electr. Overstress/ Electrostatic Discharge Symp.*, Reno, NV, USA, Oct. 1998, pp. 177–186, doi: 10.1109/EOSESD.1998.737037.

[22] M. Gartner, D. Vietzke, D. Reznik, M. Stoisiek, K. G. Oppermann, and W. Gerlach, "Bistability and hysteresis in the characteristics of segmented-anode lateral IGBTs," *IEEE Trans. Electron Devices*, vol. 45, no. 7, pp. 1575–1579, Jul. 1998, doi: 10.1109/16.701491.

[23] H. Karaca *et al.*, "Triggering of multi-finger and multi-segment SCRs near the holding voltage studied by emission microscopy under DC conditions," presented at the Int. ESD Workshop (ESDA/IEW), Hamburg, Germany, May 2021.

[24] H. Karaca *et al.*, "Simultaneous and sequential triggering in multi-finger floating-base SCRs depending on TLP pulse rise time," *IEEE Trans. Device Mater. Rel.*, vol. 20, no. 4, pp. 632–640, Dec. 2020, doi: 10.1109/TDMR.2020.3033618.

[25] K.-H. Oh, C. Duvvury, K. Banerjee, and R. W. Dutton, "Analysis of nonuniform ESD current distribution in deep submicron NMOS transistors," *IEEE Trans. Electron Devices*, vol. 49, no. 12, pp. 2171–2182, Dec. 2002, doi: 10.1109/TED.2002.805049.

[26] P. Salome, C. Leroux, J. P. Chante, P. Crevel, and G. Reimbold, "Study of a 3D phenomenon during ESD stresses in deep submicron CMOS technologies using photon emission tool," in *Proc. IEEE 35th Annu. Int. Rel. Phys. Symp.*, Denver, CO, USA, Apr. 1997, pp. 325–332, doi: 10.1109/RELPHY.1997.584282.

[27] *T.C.A.D. Industry-Standard Process and Device Simulators*, SENTAURUS, Synopsys. Inc., Mountain View, CA, USA, May 2012.

[28] B. El-Kareh and R. J. Bombard, *Introduction to VLSI Silicon Devices: Physics, Technology and Characterization*, vol. 10. New York, NY, USA: Springer, 2012.